

Magnetic field tuned anisotropic quantum phase transition in the distorted kagome antiferromagnet Nd_3BWO_9

Fangyuan Song,^{1,*} Han Ge^{2,*}, Andi Liu,¹ Yuqi Qin,¹ Yuyan Han,³ Langsheng Ling,³ Songliu Yuan,¹ Zhongwen Ouyang,¹ Jieming Sheng^{2,4,†}, Liusuo Wu,^{2,5,‡} and Zhaoming Tian^{6,§}

¹*School of Physics and Wuhan National High Magnetic Field Center, Huazhong University of Science and Technology, Wuhan 430074, China*

²*Department of Physics, Southern University of Science and Technology, Shenzhen 518055, China*

³*Anhui Province Key Laboratory of Condensed Matter Physics at Extreme Conditions, High Magnetic Field Laboratory, Chinese Academy of Sciences, Hefei 230031, China*

⁴*Spallation Neutron Source Science Center, Dongguan 523803, China*

⁵*Shenzhen Key Laboratory of Advanced Quantum Functional Materials and Devices, Southern University of Science and Technology, Shenzhen 518055, China*

⁶*Shenzhen Huazhong University of Science and Technology Research Institute, Shenzhen 518057, China*



(Received 12 August 2023; revised 21 October 2023; accepted 6 November 2023; published 13 December 2023)

Rare-earth (R) kagome-lattice magnets offer an excellent platform to discover the novel magnetic phase as well as quantum phase transition tuned by nonthermal control parameters, while the experimental realizations remain largely unexplored. Here, we report the discovery of magnetic field (B)-induced anisotropic quantum phase transition in a distorted kagome antiferromagnet Nd_3BWO_9 with $T_N \sim 0.32$ K. The isothermal magnetizations at 0.05 K exhibit the spin-flop-like metamagnetic crossover behaviors with different fractional magnetization anomalies for B perpendicular ($B||c$ axis) and parallel ($B||a^*$ axis) to the kagome plane, respectively. In combination with the thermodynamic measurements, the field-temperature (B - T) phase diagrams for both field directions are constructed and reveal the existence of several field-induced magnetic states. Along the c axis, a proximate quantum bicritical point is observed near the metamagnetic crossover, which separates the low-field antiferromagnetic (AFM) phase and the intermediate AFM phase; while, for $B||a^*$, another intermediate magnetic phase (IAFM2) appears between the low-field AFM phase and the intermediate AFM (IAFM1) phase, giving rise to a tetracritical point. These results support the anisotropic field-induced metamagnetic quantum criticalities in Nd_3BWO_9 , making it a rare kagome antiferromagnet to investigate the quantum multicriticality driven by spin frustration.

DOI: [10.1103/PhysRevB.108.214410](https://doi.org/10.1103/PhysRevB.108.214410)

I. INTRODUCTION

Rare-earth (R) based geometrically frustrated magnets (GFMs) have attracted great attention in searching for the exotic magnetic phases of matter and fractionalized spin excitations. Compared to the relatively well-studied $3d$ transition-metal systems, the materials containing $4f$ R ions have strong spin-orbital coupling, large single-ion anisotropy, dipolar exchange interaction, and rich diversity of spin types. These complex interactions and inherent lattice frustration render R -based GFMs as candidates to discover novel quantum states beyond the $3d$ -based ones including Kitaev quantum spin-liquid [1–3], quantum spin ice [4–6], and quantum dipolar phase [7]. Moreover, the relatively smaller exchange interactions between localized $4f$ moments allow an easy tunability of spin states through the disorder-free control parameters accessible in the laboratory such as external field or pressure.

As one type of spin-frustrated systems, kagome-lattice magnets with different anisotropy between the limits of isotropic Heisenberg type and Ising-like model, have attracted a lot of theoretical and experimental investigations on exploring the exotic spin states [6,8–10]. Compared to the extensive experimental studies on transition-metal kagome materials, R -based kagome magnets with considerably weaker exchange interactions have been less investigated. So far, the studied materials can be divided into two categories: one is the intermetallic compound containing conductive electrons, and the other is the insulating oxide with magnetism fully determined by the superexchange interactions of $4f$ local moments. For the former, typical examples include $R\text{AgGe}$ [11,12], $R_3\text{Ru}_4\text{Al}_{12}$ [13,14], and RPdAl [15,16] (where R = rare earth), owing to the hybridization between conductive electrons and $4f$ local moments, unconventional magnetic ground state can be generated by adjusting the Ruderman-Kittel-Kasuya-Yosida (RKKY) interaction as well as the Kondo effect between local moments [17]. For the latter, the available experimental studies are only limited to a few systems including the two-dimensional (2D) kagome $R_3\text{Sb}_3M_2\text{O}_{14}$ (M = Zn, Mg) [6,18–21] and $R_3\text{Ga}_5\text{SiO}_{14}$ (R = Pr, Nd) [22–25] families, and their magnetic ground states

*These authors contributed equally to this work.

†shengjm@sustech.edu.cn

‡wuls@sustech.edu.cn

§tianzhaoming@hust.edu.cn

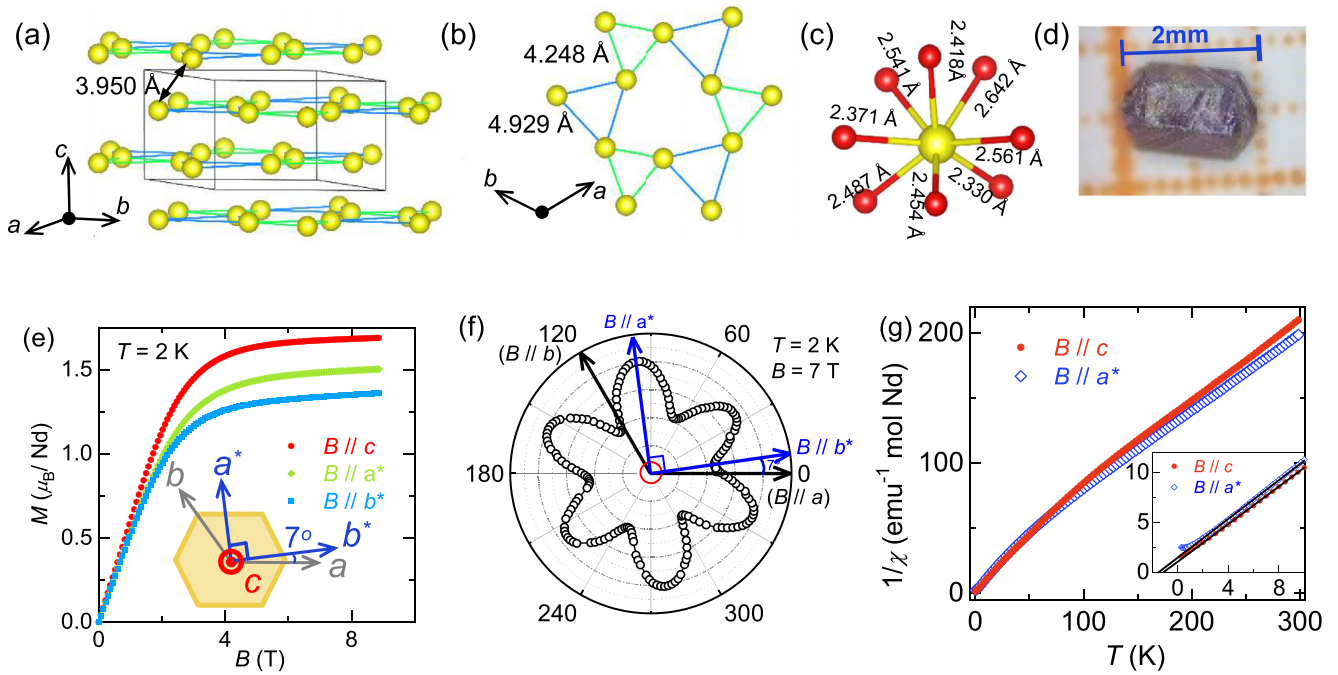


FIG. 1. Crystal structure and elementary magnetic properties of Nd_3BWO_9 single crystal. (a) The schematic view of alternating-stacked Nd-kagome layers along the c axis. (b) The distorted kagome net of Nd^{3+} ions within the ab plane. (c) The local oxygen environment of Nd^{3+} ions. (d) A typical as-grown single crystal of Nd_3BWO_9 . (e) The isothermal magnetization $M(B)$ curves at $T = 2$ K for B along the c , a^* , and b^* axes; the inset shows the definition of the c , a^* , and b^* axes. (f) The angle-dependent magnetization for B rotated within the ab plane at $T = 2$ K and $B = 7$ T; the a^* and b^* axes are along the direction with maximal and minimal magnetization values, respectively. (g) The inverse magnetic susceptibility $1/\chi(T)$ measured at $B = 1$ T over the temperature range of 0.4–300 K for $B||c$ and $B||a^*$. Inset shows the low-temperature part of $1/\chi(T)$; the solid lines show the Curie-Weiss fits in the temperature range 2–10 K.

remain to be fully understood. For example, in the distorted kagome $\text{Nd}_3\text{Ga}_5\text{SiO}_{14}$, the magnetic ground state detected by different experimental techniques seems to be confusing, where muon spin relaxation (μSR) and nuclear magnetic resonance results indicate a characteristic of spin liquid with spin fluctuating down to 60 mK [23] while the measurements of magneto-optical spectroscopy and neutron scattering support a single-ion behavior instead of spin-liquid state down to 100 mK [26,27]. For $R_3\text{Sb}_3\text{M}_2\text{O}_{14}$ compounds, the unavoidable antisite disorder between magnetic R^{3+} and nonmagnetic M^{2+} ions complicates the clarification on its intrinsic magnetic ground state [28,29], and the lack of single crystals so far hinders further detailed investigations on their exotic magnetic behaviors, especially the ones related to crystalline directions.

Despite the exploration of a novel magnetic ground state, magnetic field (B)-induced quantum phase transition (QPT) between two different ground states as a consequence of quantum correlation also attracts strong interest [30], where quantum spin fluctuations can stabilize an exotic magnetic phase or a particular spin configuration exhibiting fractional magnetization in a certain field regime. In this direction, most studies on R -based kagome materials have carried out the heavy fermion systems containing $\text{Ce}^{3+}(4f^1)$ or $\text{Yb}^{3+}(4f^{13})$ ions [17,31–36]. In these systems, both RKKY interaction and Kondo coupling can play important roles in the QPT, and consequently, they enrich the magnetic phase diagrams and in certain conditions lead to the appearance of unconventional quantum criticalities, such as the quadrupolar order and non-Fermi liquid near a quantum critical point, etc.

[33–36]. On the other hand, the competing multiple interactions complicate the underlying mechanism as an obstacle for its clarification of QPT behaviors. From this viewpoint, the insulating counterparts are more attractive to unveil the QPT dictated by the kagome-lattice topology of R^{3+} moments. Conversely, their physical clarification will help one to understand the QPT of kagome-lattice heavy fermion systems in the case of the reintroduced conductive electrons, but experimental work is rare due to the lack of an appropriate model system.

Nd_3BWO_9 belongs to one series of R -based kagome compounds $R_3\text{BWO}_9$ ($R = \text{Pr}, \text{Nd}, \text{Gd-Ho}$) crystallized in a hexagonal structure with space group $P6_3$ [37,38], where magnetic Nd^{3+} ions occupy the distorted kagome lattices in the ab -plane stacking in the “ABAB”-type fashion along the c axis [see Figs. 1(a) and 1(b)]. Thus, it provides a candidate to study the QPT phenomena in a R -based kagome insulator. In this work, through the low-temperature magnetization, specific heat, and magnetocaloric effect (MCE) measurements down to 0.05 K, we experimentally uncover the field-induced anisotropic QPTs in the Nd_3BWO_9 antiferromagnet. Below $T_N \sim 0.32$ K, the field-induced metamagnetic (MM) crossover behaviors are identified with different fractional magnetizations for B applied perpendicular ($B \perp c$) and parallel ($B \parallel a^*$) to the kagome plane, respectively. Moreover, the constructed B - T phase diagrams indicate the anisotropic multiple critical behaviors, where the metamagnetic bicritical point ($B||c$) and tetracritical point ($B||a^*$) are detected in the phase diagrams.

II. EXPERIMENTAL DETAILS

Single crystals of Nd_3BWO_9 were grown by a high-temperature flux method using Nd_2O_3 (99.99%), B_2O_3 (99.9%), and WO_3 (99.99%) as starting materials and PbO as flux, similar to the previous report [39]. The mixtures were thoroughly ground and placed in a 40-ml platinum crucible, and then heated at 1473 K for 24 h to ensure the homogeneous melting reaction. Then, the temperature was cooled slowly to 1073 K at a rate of 2 °C. The crystals can be separated by the mechanical exfoliation method [a photograph of as-grown Nd_3BWO_9 single crystal is shown in Fig. 1(d)]. Also, the La_3BWO_9 samples were synthesized, using as the nonmagnetic reference of specific heat for Nd_3BWO_9 single crystal. The crystal structure was characterized by x-ray diffraction using a Bruker D8 x-ray machine with $\text{Cu K}\alpha$ radiation ($\lambda = 1.5418 \text{ \AA}$) using the powders from the crashed crystals. Also, the crystal structure was determined by single-crystal x-ray diffraction with the diffraction data collected by a Kappa Apex2 CCD diffractometer (Bruker) using graphite-monochromated $\text{Mo K}\alpha$ radiation ($\lambda = 0.71073 \text{ \AA}$). The obtained crystal data from the structure refinements are provided in Tables S1 and S2 in the Supplemental Material [40].

Temperature-dependent dc susceptibility $\chi(T)$ and isothermal magnetization $M(B)$ measurements were performed on the Quantum Design superconducting quantum interference device magnetometer and commercial physical property measurement system (PPMS) for the temperature range of 1.8–300 K. For the lower temperatures ($0.05 \leq T \leq 4 \text{ K}$), magnetic measurements were carried out using a Hall sensor magnetometer integrated with a dilution insert of the PPMS. The specific heat and MCE were measured down to 0.06 K in a PPMS equipped with a dilution refrigeration system using the heat-capacity option. Heat-capacity measurements were carried out under constant field by the thermal relaxation method, and MCEs were measured under quasi-adiabatic conditions using a constant field sweeping rate of 20 Oe/s between 0 and 3 T. The thermometer resistance of the heat-capacity thermometer was measured and converted to temperatures, and then the MCE values can be derived.

III. RESULTS AND DISCUSSIONS

A. Low-temperature magnetic ground state

The refined crystal structure of Nd_3BWO_9 fits the hexagonal $P6_3$ space group with lattice parameters $a = b = 8.695(2) \text{ \AA}$ and $c = 5.485(1) \text{ \AA}$, consistent with the previous results [37]. The detailed information on atomic coordinates and bond distances from the single-crystal refinements are listed in Tables S1 and S2. In the unit cell, magnetic Nd^{3+} ions are located on the distorted dodecahedron site surrounded by eight oxygens with completely different Nd-O bond distances [see Fig. 1(c)]. Through the corner- or edge-sharing interconnections with WO_6 octahedra and planar BO_3 groups, NdO_8 polyhedra are linked to form a distorted “breathing” kagome network within the ab plane. The side lengths of the Nd^{3+} equilateral triangles are $r_1^{\text{intra}} = 4.248 \text{ \AA}$ and $r_2^{\text{intra}} = 4.929 \text{ \AA}$, which are slightly larger than the interlayer’s separation $r^{\text{inter}} = 3.950 \text{ \AA}$. Using the side length of Nd^{3+} equilateral

triangles, the distortion value of the breathing kagome lattice is evaluated to $\frac{r_2^{\text{intra}} - r_1^{\text{intra}}}{\frac{r_2^{\text{intra}} + r_1^{\text{intra}}}{2}} \times 100\% \sim 7.4\%$ and that is larger than the value $\sim 2.6\%$ in the distorted kagome $\text{Nd}_3\text{Ga}_5\text{SiO}_{14}$ [22]. From the structure viewpoint, another important feature is the large difference of ionic radii and distinct local oxygen coordination environments between magnetic Nd^{3+} and nonmagnetic $\text{B}^{3+}/\text{W}^{6+}$ cations, which can minimize the antisite disorder. Compared to the kagome $R_3\text{Sb}_3\text{M}_2\text{O}_{14}$ ($M = \text{Zn}, \text{Mg}$) systems, the antisite disorder between RE^{3+} and M^{2+} ions impedes the clarification of an intrinsic magnetic ground state [28,29]; here the weak disorder effect lets Nd_3BWO_9 act as a clean system to study the intrinsic kagome magnetism.

The isothermal magnetization $M(B)$ measurements at 2 K on Nd_3BWO_9 single crystals have been carried out for B along the c , a^* , and b^* axes; the definition of axis direction is schematically shown in the inset of Fig. 1(e). The $M(B)$ results indicate a magnetic anisotropy; the c -axis magnetization has the largest saturated magnetization $M_s \sim 1.71 \mu_B/\text{Nd}$. As B rotates within the ab plane [see Fig. 1(f)], angle-dependent magnetizations show a sixfold symmetry; accordingly, the a^* and b^* axes are along the direction exhibiting the maximum and minimum moment values. In this definition, the a^* axis tilts from the crystallographic b axis by a canting angle $\sim 7^\circ$ within the ab plane. Figure 1(g) shows the inverse magnetic susceptibilities $\chi^{-1}(T)$ along the c and a^* axes; the high-temperature ($T > 150 \text{ K}$) Curie-Weiss (CW) fits give the CW temperature $\theta_{\text{CW}} = -39.7 \text{ K}$ ($B \perp c$) and $\theta_{\text{CW}} = -38.2 \text{ K}$ ($B \parallel a^*$) and effective moment $\mu_{\text{eff}} = 3.59 \mu_B$ ($B \perp c$) and $\mu_{\text{eff}} = 3.68 \mu_B$ ($B \parallel a^*$), respectively. The obtained μ_{eff} are close to the free-ion value of $3.62 \mu_B$ for the Nd^{3+} ($4f^3$, $J = 9/2$) ion, but a large value of $|\theta_{\text{CW}}|$ does not indicate strong antiferromagnetic (AFM) interactions between Nd^{3+} moments due to the thermal population of excited crystal electric field (CEF) levels [37,41]. Thereby, the CW fitting is also performed at low temperatures $T < 10 \text{ K}$ [see the inset of Fig. 1(g)], which gives effective moments $\mu_{\text{eff}} = 2.92 \mu_B$ ($B \perp c$) and $\mu_{\text{eff}} = 2.85 \mu_B$ ($B \parallel a^*$). The low-temperature fitted $\theta_{\text{CW}} = -0.97 \text{ K}$ ($B \parallel c$) and $\theta_{\text{CW}} = -1.31 \text{ K}$ ($B \parallel a^*$) reveal the dominant AFM interactions between Nd^{3+} moments on the order of a kelvin.

To determine the magnetic ground state, zero-field specific heat $C_p(T)$ of Nd_3BWO_9 with temperature down to 0.1 K is shown in Fig. 2(a). The typical feature is the broad maximum centered at $T_s \sim 0.85 \text{ K}$ and the λ -like peak at $T_N \sim 0.32 \text{ K}$; the latter signals the onset of an AFM ordered state. Below 0.15 K, the upturn of $C_p(T)$ comes from the contribution of a hyperfine field enhanced by a nuclear Schottky anomaly (C_{Nuc}); the gray dashed line in Fig. 2(a) shows the estimation by $C_{\text{Nuc}} \propto 1/T^2$ in a first approach. After further subtraction of the lattice contribution (C_{Latt}) using the nonmagnetic analog La_3BWO_9 as background, the magnetic specific heat $C_M(T)$ of Nd_3BWO_9 is obtained as plotted in Fig. 2(b). Besides the two peaks at T_N and T_{sr} , another high- T broad hump maximized at $\sim 72 \text{ K}$ is visible, which is associated with the Schottky anomaly with CEF energy splitting of the $J = 9/2$ multiplet of Nd^{3+} ions. From the fit to $C_M(T)$ data by the two-level model, the first CEF excited level is estimated to be $\sim 13 \text{ meV}$; this large energy gap ensures the well-separated Kramers doublet ground state from the first excited state. Thus, Nd_3BWO_9 can be well considered as an effective $S_{\text{eff}} =$

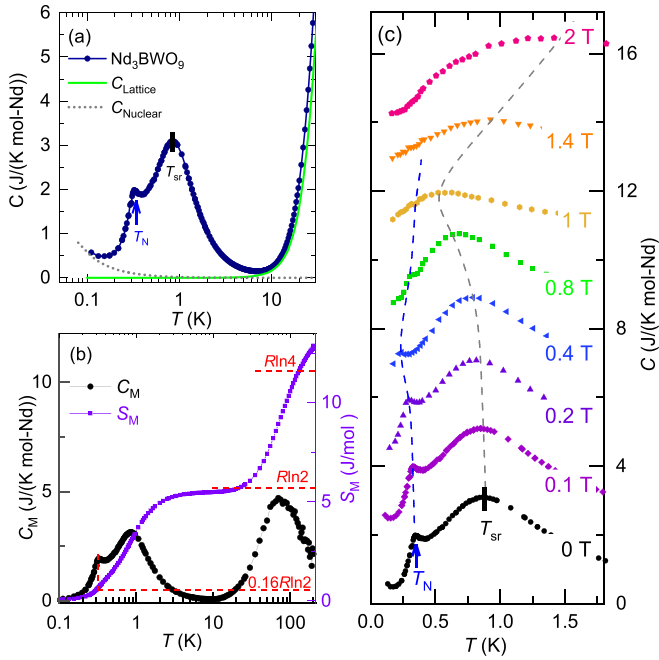


FIG. 2. (a) Zero-field specific heat $C_p(T)$ of Nd_3BWO_9 (solid circles) and La_3BWO_9 (green line); the dashed gray line shows the estimated contribution from nuclear Schottky effect. The T_N and T_{sr} are marked by the arrow and vertical line, respectively. (b) Zero-field magnetic specific heat $C_M(T)$ and associated magnetic entropy $S_M(T)$ of Nd_3BWO_9 . (c) Low-temperature specific heat $C_p(T)$ at different magnetic fields along the c axis; each data set is offset by $2 \text{ J}/(\text{K mol} - \text{Nd})$ for clarification; the dashed blue and gray lines guide the evolution of T_N and T_{sr} in $C_p(T)$ under magnetic field.

$1/2$ moment system in the low-temperature and low-field regimes.

The magnetic entropy $S_M(T)$ evaluated by integrating C_{mag}/T over temperature is shown in Fig. 2(b). As T is increased, $S_M(T)$ reaches a saturation value $\sim R \ln 2$ at 10 K as expected for the doublet ground state. While the release of magnetic entropy at T_N only reaches $\sim 0.16R \ln 2$, this implies the strong spin fluctuation in the temperature range of $T_N < T < 10 \text{ K}$ and which prevents a total ordering of Nd^{3+} moments; then the broad peak at T_{sr} is ascribed to the short-range spin correlation. By applying a magnetic field ($B||c$), both T_N and T_{sr} show the nonmonotonic temperature dependencies as guided by the dashed lines in Fig. 2(c). As increased $B \geq 1 \text{ T}$, T_N is suppressed to below 0.1 K and the system enters the fully polarized (FP) state.

B. Field-induced metamagnetism and fractional magnetizations

Figures 3(a)–3(f) show the isothermal $M(B)$ and its field derivative dM/dB curves at low temperatures of $0.05 \text{ K} \leq T \leq 2 \text{ K}$ for B along the three typical axes. At $T = 50 \text{ mK}$, all $M(B)$ curves reach the saturations at small field $B_s < 1.2 \text{ T}$ with magnetic moments $M_{s,c} = 1.77\mu_B/\text{Nd}$, $M_{s,a^*} = 1.50\mu_B/\text{Nd}$, and $M_{s,b^*} = 1.32\mu_B/\text{Nd}$ for B along c , a^* , and b^* , respectively. Comparing the $M(B)$ and dM/dB curves, we can identify an obvious magnetic anisotropy. For $B||c$, the $M(B)$ curves exhibit the spin-flop-like MM transition with

an inflection point between the critical fields $B_{c1} \sim 0.54 \text{ T}$ and $B_{c2} \sim 0.65 \text{ T}$, where B_{c1} and B_{c2} are determined by the peak of the dM/dB curves [see Fig. 3(b)]. Following this metamagnetic transition, magnetization shows a weak step at $1/3 M_{s,c}$, then it increases steeply and approaches its saturation at $B > B_s$. By contrast, for $B||a^*$, two successive metamagnetic transitions are detected with critical fields $B_{a^*1} \sim 0.49 \text{ T}$ and $B_{a^*2} \sim 0.63 \text{ T}$, where the $M(B)$ curves show two fractional magnetization anomalies at $\sim 1/6 M_{s,a^*}$ and $\sim 1/4 M_{s,a^*}$ [see Figs. 3(c) and 3(d)]. Also, a similar $1/4$ magnetization anomaly is observed along the b^* axis. These results demonstrate the anisotropic metamagnetism evidenced by the $1/3$ - and $1/4$ -fractional magnetizations for B perpendicular and parallel to the kagome plane, respectively. Here, it is noteworthy that the in-plane $1/4 M_s$ in Nd_3BWO_9 is distinct from the $1/3 M_s$ in uniform kagome AFMs [42–44]. For the emergence of fractional magnetization under magnetic field in kagome-lattice magnets, recent theoretical studies have revealed the important roles of lattice distortion on the diversity of fractional magnetizations where different spin configurations can be stabilized by tunable spin-lattice coupling and spatial exchange anisotropy [45,46]. Herein, the in-plane $1/4$ -fractional magnetization can be ascribed to the anisotropic planar magnetic interactions inherent in the distorted breathing kagome lattice of Nd^{3+} moments, leading to a magnetic structure with interspin angle deviating from 120° under magnetic field. This is in accordance with the recent theoretical analysis on the R -kagome spin system [46], where the $1/6 M_s$ and $1/4 M_s$ can be induced by the lattice deformation under in-plane field.

As temperature is increased, the dM/dB peaks near the metamagnetic crossover become weak and then disappear at $T > T_N$, while the anomalies at $\sim B_s$ survive up to $T > 1 \text{ K}$. To get more information on the low- T magnetic behavior, magnetic susceptibilities $\chi(T)$ in the temperature range of 0.04 – 3 K are presented for B along the c and a^* axes in Figs. 4(a) and 4(b). The $\chi(T)$ taken at $B = 0.2 \text{ T}$ exhibits a rounded maximum at $T_{sr} \sim 1.2 \text{ K}$, signifying the short-range spin correlation usually observed in the low-dimensional spin-frustrated systems [3,47]. Additionally, T_N can be determined by the maxima in the $\chi(T)$ curves at intermediate fields ($0.4 \text{ T} < B < 0.8 \text{ T}$) denoted by arrows in Figs. 4(a) and 4(b). As B is increased, it moves to low temperature and becomes undistinguishable for $B > B_s$ when it enters the FP magnetic state.

C. Field-temperature magnetic phase diagrams

To establish the phase boundaries of B -induced phase transitions in Nd_3BWO_9 , the isothermal field scans on specific heat $C_M(B)$ were measured at different temperatures for B along the c and a^* axes; the representative $C_M(B)/T$ data are plotted in Figs. 5(a)–5(d). Along these two field directions, two anomalous peaks can be identified near the critical fields as the field across the metamagnetic transition in the $C_M(B)/T$ curves at temperatures $0.1 \text{ K} < T < T_N$, which are separated from the low- T single peak at $T < 0.1 \text{ K}$ ($B||c$) and $T = 0.12 \text{ K}$ ($B||a^*$) [see Figs. 5(a) and 5(c)]. Upon increasing T , these two critical fields shift in opposite directions, then the “double hump” shaped anomaly flattens into a “wing” shape

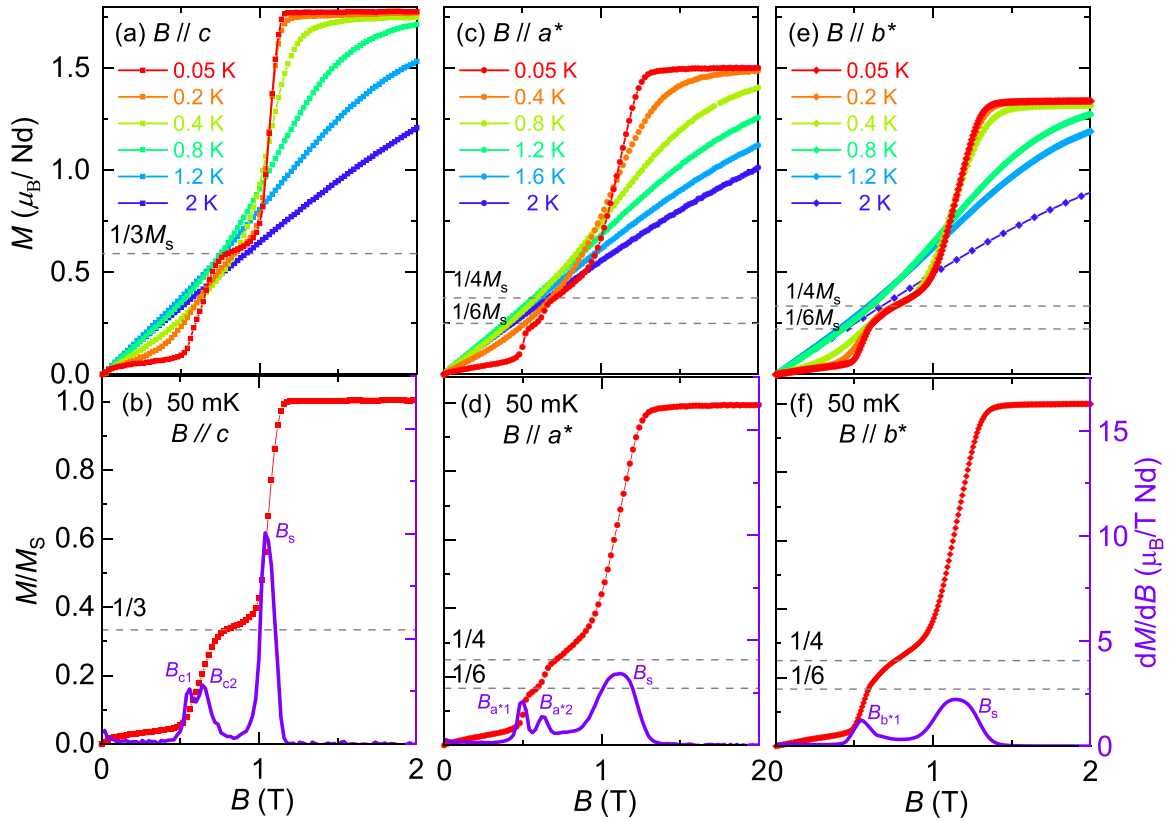


FIG. 3. The isothermal field-dependent magnetization $M(B)$ curves of Nd_3BWO_9 single crystal at low temperatures ($0.05 \text{ K} \leq T \leq 2 \text{ K}$) for (a) $B \parallel c$; (b) $B \parallel a^*$ and (c) $B \parallel b^*$, respectively. The normalized magnetization (M/M_s) and the derivative of magnetization (dM/dB) curves at 50 mK for (d) $B \parallel c$, (e) $B \parallel a^*$, and (f) $B \parallel b^*$, respectively.

when T is close to T_N , as exemplarily shown for the data of $T = 0.3 \text{ K}$ [see Figs. 5(b) and 5(d)]. At the high-field sides, another anomaly located at $\sim B_s$ is visible for $T \leq 0.2 \text{ K}$, and it splits into two broad peaks whose magnitudes gradually decrease with increased T . Moreover, these two peaks are extended well above T_N characterizing a field-induced magnetic crossover behavior. The peak positions ($B_{s1,c}$, $B_{s2,c}$ for $B \parallel c$ and B_{s1,a^*} , B_{s2,a^*} for $B \parallel a^*$) are used to determine the phase boundaries of magnetic crossover.

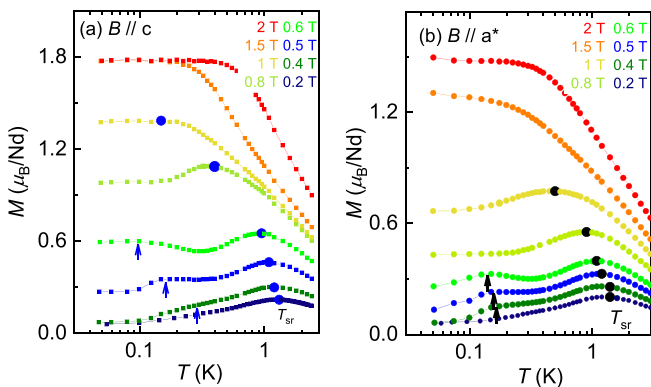


FIG. 4. The low-temperature magnetization $M(T)$ curves of Nd_3BWO_9 single crystal at different fields for (a) $B \parallel c$ and (b) $B \parallel a^*$; the arrow and solid circles indicate the positions of T_N and T_{sr} in the $M(T)$ curves.

By combining all the available susceptibility, magnetization, and specific-heat data, we construct the B - T phase diagrams based on the critical fields and ordering temperatures. The contour plots using the $C_M(B)$ data for $B \parallel c$ and $B \parallel a^*$ are shown in Figs. 6(a) and 6(b), respectively. For $B \parallel c$, two critical points can be identified in the phase diagram: one is the bicritical point (BCP) as observed in anisotropic AFMs with metamagnetic transition [48,49]; at this point ($B_{\text{BCP}} \sim 0.61 \pm 0.02 \text{ T}$, $T_{\text{BCP}} \sim 0.03 \pm 0.02 \text{ K}$) two critical lines labeled by $T_{N,c1}(B)$ and $T_{N,c2}(B)$ converge; another is a tricritical point (TCP) at $B_{s,c} \sim 1.03 \pm 0.02 \text{ T}$ and $T_{\text{TCP}} \rightarrow 0.18 \pm 0.02 \text{ K}$, where the paramagnetic (PM) phase, intermediate AFM (IAFM) phase, and FP phase meet. A careful inspection on the location of the BCP reveals that T_{BCP} is quite close to 0 K, and this is supported by the low- T $M(B)$ curves since the BCP should reside at a field between $B_{c1} \sim 0.54$ and $B_{c2} \sim 0.65 \text{ T}$ and temperature below the base temperature of 50 mK (far lower than T_N) [see Fig. 3(b)]. Thus, it realizes a proximate quantum bicritical point (QBCP) [35,50], around which the observed dip behavior of the $T(B)$ curve [see Fig. 7(a)] supports the presence of large quantum fluctuation as discussed later. In this case, the spin-flop line below the BCP shrinks to a single point at $T = 0 \text{ K}$. On the high-field side, below the TCP, a nearly vertical critical line separating the IAFM and FP phases is observed. At elevated temperatures ($T > T_{\text{TCP}}$), it splits into two critical lines forming a V-shaped critical regime [see Fig. 6(a)]. Additionally, we can find a dome-shaped phase region mapped by B_{c2}

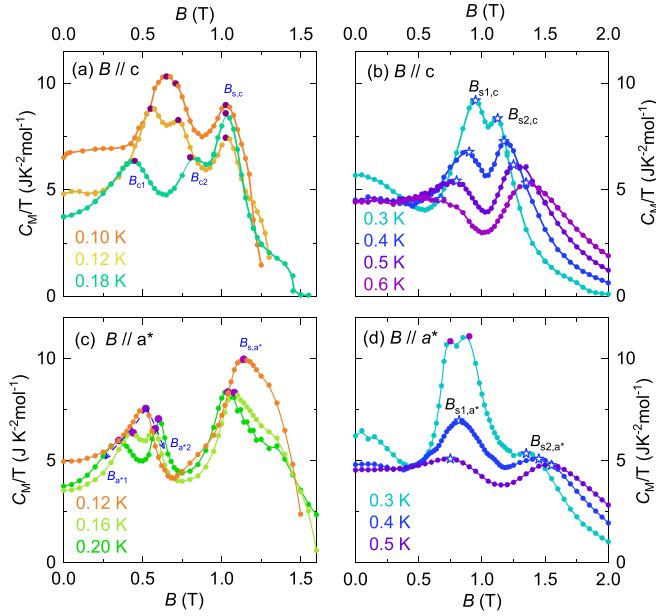


FIG. 5. Field dependence of specific heat $C_M(B)$ of Nd_3BWO_9 single crystal at selected temperatures (a) $T < 0.2$ K and (b) $T > 0.3$ K for $B||c$, (c) $T < 0.2$ K, and (d) $T > 0.3$ K under $B||a^*$. The solid circles and open stars indicate the field positions for the peaks of $C_M(B)/T$ curves, where B_{c1} , B_{c2} and B_{a*1} , B_{a*2} are the metamagnetic critical fields and $B_{s1,c}$, $B_{s2,c}$ and B_{s1,a^*} , B_{s2,a^*} indicate the critical fields of magnetic crossover at high fields.

and $B_{s,c}$, inside which the $1/3 M_{s,c}$ plateau emerges. In all, the above c -axis phase diagram of Nd_3BWO_9 highlights the realization of the quantum bicriticality previously reported in the distorted kagome metals YbAgGe [34] and CeRhSn [35] but not yet in insulating counterparts. In the above kagome metallic systems, the occurrence of a QBCP is proposed to be driven by two controlling parameters with dedicated strengths [34,35,51]: one is the ratio of Kondo coupling to RKKY interaction and another is quantum fluctuation by spin frustration; the tunability on both parameters can lead to the appearance

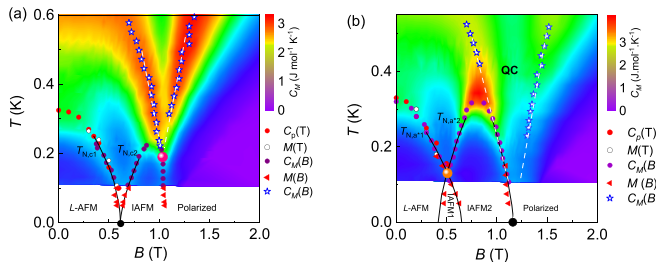


FIG. 6. The magnetic phase diagrams of Nd_3BWO_9 single crystal. (a) The B - T phase diagram for $B||c$; the black and dashed gray lines show the fits of phase boundaries by power law; the quantum bicritical point (QBCP) and tricritical point (TCP) are denoted by the black ball and pink ball, respectively. (b) The B - T phase diagram for $B||a^*$; the tetracritical point (TP) and quantum critical point (QCP) are denoted by the orange ball and black ball, respectively. The points on the phase boundaries are determined by magnetic susceptibility, magnetization, and specific-heat results.

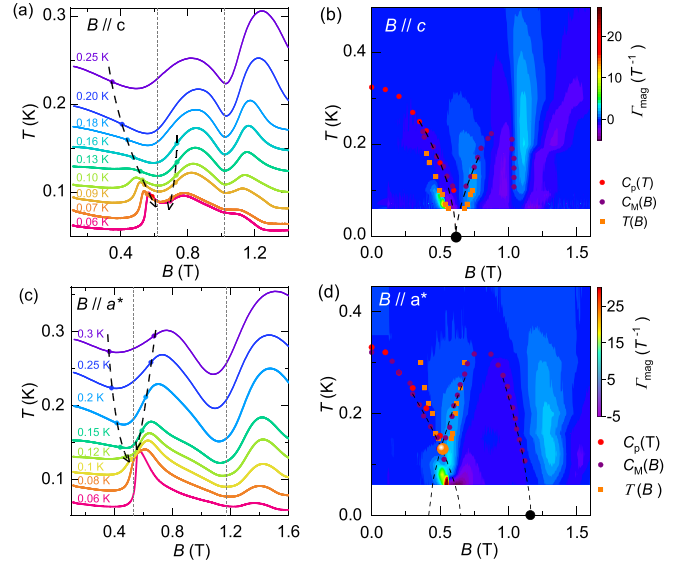


FIG. 7. (a) Magnetocaloric effect $T(B)$ results at different temperatures measured in the adiabatic condition and (b) the contour plot of the B - T phase diagrams using the calculated $\Gamma_{\text{mag}}(B)$ from the $T(B)$ data for $B||c$. (c) The $T(B)$ data and (d) the contour plot of the B - T phase diagrams using the $\Gamma_{\text{mag}}(B)$ results for $B||a^*$. In (a) and (c), the arrows guide the evolution of phase boundaries determined by the peaks of dT/dB near the metamagnetic crossover; the dashed lines indicate the field positions of the CPs. In (b) and (d), the phase boundaries are determined by magnetocaloric effect and specific heat; the dashed lines represent the power-law fits to the phase boundary lines.

of QBCP. In Nd_3BWO_9 , due to the absence of conductive electrons, the observed quantum bicriticality should be related to the large quantum fluctuation enhanced by magnetic frustration; its existence is indicated by the low-temperature $C_M(T)$ and $S_M(T)$ results with only $\sim 16\%$ of magnetic entropy released below T_N .

The phase diagrams of $B||a^*$ are shown in Fig. 6(b). Despite the PM regime, four magnetic ordered phases can be identified: the low-field AFM (L -AFM) phase below $B_{a*1} \sim 0.49$ T, the IAFM1 phase in a narrow field range between $B_{a*1} \sim 0.49$ T and $B_{a*2} \sim 0.68$ T, the IAFM2 phase ended at $B_{s,a*}$, and the high-field FP phase at $B > B_{s,a*}$. Between the IAFM2 and FP phases, a QCP is identified at $B_{s,a*} \sim 1.16 \pm 0.03$ T and $T_{\text{CP}} \rightarrow 0$ K; above that there exists a phase region between the phase boundaries of magnetic crossover as denoted by the dashed lines. Compared to $B||c$, the most distinct difference happens near the metamagnetic crossover; the BCP turns out to be a tetracritical point (TP) at which four phase critical lines meet together [52,53]. The TP is located at $B_{\text{TP}} \sim 0.51 \pm 0.02$ T and $T_{\text{TP}} \sim 0.13 \pm 0.02$ K; above that, two order-disorder transition lines [$T_{N,a*1}(B)$ and $T_{N,a*2}(B)$] separate the PM phase between the L -AFM and IAFM2 phases. Below the TP, another two critical lines separate the IAFM1 phase from the L -AFM and IAFM2 phases; this is different from the occurrence of a spin-flop transition line in the bicritical phase diagram [48,54]. The formation of a novel IAFM1 phase is in accordance with the a^* -axis $M(B)$ curves at 50 mK, which display two-stage fractional magnetization

steps in contrast to the single $1/3M_s$ anomaly for $B||c$ (further comparison is shown in Fig. S2). Correspondingly, the $1/6M_{s,a^*}$ and $1/4M_{s,a^*}$ anomalies occur inside the IAFM1 and IAFM2 phases in the phase diagrams, respectively.

To characterize the metamagnetic critical behaviors, the phase boundaries are analyzed by a power law with the form $T_N(B) \propto |B - B_c|^\phi$, where B_c is the critical field and ϕ is the critical exponent. Along the c axis, by fixing $B_c = B_{\text{BCP}} = 0.61(1)$ T and $T_c = 0$ K, the fits to $T_{N,c1}(B)$ and $T_{N,c2}(B)$ yield two critical exponents $\phi_{c1} = 0.52(2)$ and $\phi_{c2} = 0.61(2)$, signifying a change of spin symmetry or dimensionality across the metamagnetic BCP [53]. Also, the fits to $T_{N,c1}(B)$ and $T_{N,c2}(B)$ with the constraint of $\phi_{c1} = \phi_{c2} = \phi_c$ is possible, which gives $\phi_c = 0.55(2)$. For $B||a^*$, the corresponding estimation with $B_c = B_{\text{TP}} = 0.61(1)$ T gives the critical exponent $\phi_{a^*} = 0.63(2)$ [see the dashed lines in Fig. 6(b)], and this exponent value is coordinated by the fitted value $\phi_{a^*,s} = 0.65(2)$ near the high-field QCP using $B_c = B_{s,a^*} \sim 1.16$ and $T_{\text{CP}} = 0$ K. Along these two directions, different critical exponents suggest the anisotropic scaling behaviors; the exponent $\phi_c = 0.55(2)$ for $B||c$ is in better agreement with the three-dimensional (3D) Ising anisotropy with $\phi = 1/2$ [55], while $\phi_{a^*} = 0.63(2)$ along the a^* axis coincides with the expected value $\phi = 2/3$ of the 3D XY universality as reported in the spin-dimerized $\text{BaCuSi}_2\text{O}_6$ [56] and spin-frustrated Cs_2CuCl_4 AFMs [57].

D. Thermodynamic evidence of multiple quantum criticality

To get more experimental evidence on the quantum criticality, we carried out the MCE measurements under quasiadiabatic conditions, which can reflect the sample-temperature change induced by the evolution of magnetic entropy under field sweeping. The collected $T(B)$ data measured at different initial temperatures (T_{ini}) for the $B||c$ and $B||a^*$ axes are shown in Figs. 7(a) and 7(c), respectively. Along the c axis, the $T(B)$ curves exhibit dramatic temperature drops as approaching the CPs. For $T_{\text{ini}} < T_N$, we can observe a clear temperature diplike feature near the critical fields $B_{\text{BCP}} \sim 0.61$ T and $B_{\text{TCP}} \sim 1.03$ T, where the accumulation of magnetic entropy $S_M(B)$ reaches its maximum. Below the TCP, the first-order type phase transition for $T_{\text{ini}} < \sim 0.15$ K is indicated by an asymmetric peaklike feature of $T(B)$ curves due to the consequence of entropy discontinuity. For $B||a^*$, in temperature regimes $0.12 \text{ K} \leq T_{\text{ini}} \leq 0.5$ K, the $T(B)$ curves also exhibit similar temperature drop behavior close to the TP. As $T_{\text{ini}} < 0.1$ K, the temperature diplike feature is gradually suppressed reflecting the reduced accumulation of $S_M(B)$ at the field around B_{TP} . At $T_{\text{ini}} = 0.06$ K, a pronounced temperature peak appears at ~ 0.56 T well below the TP, and around which field the $M(B)$ curves show a $1/6M_{s,a^*}$ anomaly [see Figs. 3(c) and 3(d)].

The magnetic Grüneisen parameter derived from the adiabatic MCE $\Gamma_B(B) = 1/T(dT/dB)$ has been shown to be a suitable probe to identify the QCPs [58]. Figures 7(b) and 7(d) show the obtained $\Gamma_B(B)$ results for $B||c$ and $B||a^*$, respectively. Along both field directions, as approaching the CPs, the $\Gamma_B(B)$ curves exhibit the singularities with sign change in accordance with the criticality-enhanced MCE [58–60]. To illustrate the multiple quantum criticalities, the B - T phase

diagrams are mapped out by the contour plots of the $\Gamma_B(B)$ data, where the phase boundaries are determined by the peak positions of the dT/dB curves shown in Figs. 7(b) and 7(d). As seen, the obtained overall phase diagrams and extracted phase boundaries agree well with those by the specific-heat and magnetization data. In the c -axis phase diagram, the position of the metamagnetic BCP from the linear extrapolation of B_{c1} and B_{c2} goes to zero temperature, consistent with the realization of a QBCP. A peak of $\Gamma_B(B)$ centered at ~ 1.1 T and ~ 0.18 K suggests a TCP, and the location of the TCP is consistent with the determination by the fields $B_{s1,c}$ and $B_{s2,c}$ of magnetic crossover as shown in Fig. S3. By contrast, for $B||a^*$, the high-field CP resides at zero temperature and around which there exists a quantum critical regime at finite temperatures, the metamagnetic TP appears at finite temperature, below which an enclosed IAFM1 phase region occurs.

IV. DISCUSSIONS AND CONCLUSIONS

It is interesting to compare the magnetic behaviors of Nd_3BWO_9 with those observed in other R -based kagome-lattice systems. For its magnetic ground state, the coexistence of long-range magnetic order and large spin fluctuation is quite different from the kagome lattice $\text{Nd}_3\text{Sb}_3\text{Mg}_2\text{O}_{14}$ with a single magnetic phase transition at $T_N \sim 0.54$ K [19,21] and the distorted kagome $\text{Nd}_3\text{Ga}_5\text{SiO}_{14}$ with a spin disorder ground state [23,27]. In terms of field-induced QPT, it is compared with the kagome-lattice heavy fermion systems with hexagonal ZrNiAl -type crystal structure [16,34–36,61], which provide the rare examples exhibiting field-induced metamagnetic quantum criticalities similar to the observation in Nd_3BWO_9 . But, these two are quite distinct, as the former can be tuned by the RKKY interaction and Kondo coupling, whereas the above two kinds of interactions are completely absent in Nd_3BWO_9 due to its insulating nature. Based on this consideration, the anisotropic multicritical behaviors should be related to the strong quantum spin fluctuation driven by frustration with an anisotropic form, and indeed the low- T fitted $\theta_{\text{CW}} = -0.97$ K ($B||c$) and $\theta_{\text{CW}} = -1.31$ K ($B||a^*$) support the exchange anisotropy with magnetic frustration index $f = |\theta_{\text{CW}}/T_N| = 3.0$ ($B||c$) and $f = 4.1$ ($B||a^*$), respectively. Moreover, the nearest-neighboring (NN) dipolar interaction (D) and magnetic exchange coupling (J_{NN}) can be evaluated by the following relations [5,20]: $D = \frac{-\mu_0\mu_{\text{eff}}^2}{4\pi r_{\text{NN}}^3}$ and $\theta_{\text{CW}} = -\frac{zJ_{\text{NN}}S_{\text{eff}}(S_{\text{eff}}+1)}{3k_B}$, where μ_{eff} is the low-temperature fitted effective moment, r_{NN} is the NN distance of Nd ions, and z is the number of nearest-neighbor spins, respectively. The obtained interplane dipolar interaction $D_{\text{inter}} = 0.08$ K and exchange interaction $J_{\text{NN}}^{\text{inter}} = -0.65$ K alongside the intraplane dipolar interaction $D_{\text{intra}} = 0.06$ K and the exchange interaction $J_{\text{NN}}^{\text{intra}} = -1.31$ K support the existence of anisotropic magnetic interactions along different axes. From the structure viewpoint, the AB-type kagome-lattice topology of Nd^{3+} moments and their magnetic exchange pathways can account for this anisotropy, where the nearest-neighboring Nd-Nd ions form the zigzag chain structure along the c axis and the breathing kagome-lattice connections within the ab plane. For the above two types of spin-lattice topology, since each one can independently generate quantum spin fluctuation, their

intertwining will consequently generate the 3D anisotropic exchange interaction as well as quantum spin fluctuation. Further considering the low site symmetry around Nd^{3+} ions [37,62], the Nd-O-Nd exchange pathways exhibit different bond distances and bond angles within or perpendicular to the ab plane, and also contribute to the magnetic anisotropy.

For the metamagnetic bicriticality, the phase diagram analysis on R -based frustrated heavy systems have revealed that both Kondo effect and spin frustration can be effective parameters on tuning the location of metamagnetic CPs [34,51], which depends on their strengths. According to that scenario, for $B||c$, the tuning parameter of the QBCP in Nd_3BWO_9 can be related to the quantum fluctuation by a moderate frustration strength with $f = 3.0$, then by reducing and enhancing the strength of magnetic frustration, it is expected to generate a finite-temperature BCP as observed in anisotropic AFMs without apparent magnetic frustration and metamagnetic spin disorder state existing at finite interval field regimes. For the former situation, a finite-temperature critical end point associated with a first-order quantum transition line was recently observed in the frustrated Shastry-Sutherland-lattice and pyrochlore-lattice magnets [63,64], that terminates a first-order metamagnetic transition line. For the latter case, a field-induced intermediate quantum spin-liquid phase at finite interval fields has been proposed in kagome systems [16,34,36,65], which calls for further experimental study in the future.

Compared to $B||c$, a tetracritical phase diagram is realized for $B||a^*$. For the appearance of a tetracritical point, it was initially predicted in the anisotropic 3D Heisenberg AFMs as well as randomly mixed magnets [52,53,66]. In those systems, distinct to the first critical line separating two ordered phases below the BCP in the bicritical phase diagram, an intermediate magnetic phase can be stabilized which exhibits the simultaneous ordering of two spin components (diagonal and off-diagonal moments) below the TP, and which phase can be called a spin analog of supersolid state due to the simultaneous breaking of discrete lattice translation symmetry and spin rotational symmetry [48,49]. As one typical spin system with tetracritical point, a two-dimensional uniaxial AFM with cubic anisotropy [67], the appearance of a tetracritical point refers to a situation in which two types of critical lines encompassing distinct order parameters (Ising line and XY Kosterlitz-Thouless line) intersect at finite temperature, that will enclose a novel intermediate phase. Here, the easy

c -axis magnetization and the accompanying in-plane sixfold magnetic anisotropy support the Nd_3BWO_9 to be a 3D AFM with Ising anisotropy. Along the a^* axis, the observation of $1/6M_S$ in $M(B)$ curves corresponds to this novel intermediate phase possibly stabilized by the intraplane breathing kagome lattice, and even its nature and related spin configurations still need to be clarified. In light of this, the single-crystal neutron scattering at low temperatures is required. More interestingly, to explore the potential novel magnetic states and multicritical points, another important investigation is the synthetic tunability on the spin frustration strength through the combination of magnetic field and other nonthermal parameters including chemical doping, pressure, as well as uniaxial strain.

In summary, the distorted kagome antiferromagnet Nd_3BWO_9 gives experimental access to investigate the field-induced quantum phase transition. Below $T_N \sim 0.32$ K, our isothermal magnetizations reveal the different metamagnetic crossover behaviors with the observation of a $1/3$ -fractional magnetization for $B||c$ and two successive fractional magnetization ($1/6M_S$, $1/4M_S$) anomalies for $B||a^*$, respectively. In combination with the thermodynamic results, the constructed B - T magnetic phase diagrams establish the anisotropic multicritical behaviors with the detection of a metamagnetic bicritical point ($B||c$) and a tetracritical point ($B||a^*$). The above field-induced quantum criticalities in Nd_3BWO_9 open up the possibility to explore the multiple QCs tuned by the nonthermal parameters.

ACKNOWLEDGMENTS

We thank Wei Li and Gang Chen for valuable discussions. We acknowledge financial support from the National Natural Science Foundation of China (Grants No. 11874158 and No. U20A2073), the Fundamental Research Funds of Guangdong Province (Grant No. 2022A1515010658), and Guangdong Basic and Applied Basic Research Foundation (Grant No. 2022B1515120020). A portion of this work was carried out at the synergetic extreme condition user facility and a portion of the magnetic measurements was performed on the Steady High Magnetic Field Facilities. We would like to thank the staff of the analysis center of Huazhong University of Science and Technology for their assistance in structural characterizations.

-
- [1] H. Takagi, T. Takayama, G. Jackeli, G. Khaliullin, and S. E. Nagler, Concept and realization of Kitaev quantum spin liquids, *Nat. Rev. Phys.* **1**, 264 (2019).
- [2] J. Xing, E. Feng, Y. Liu, E. Emmanouilidou, C. Hu, J. Liu, D. Graf, A. P. Ramirez, G. Chen, H. Cao, and N. Ni, Néel-type antiferromagnetic order and magnetic field-temperature phase diagram in the spin-1/2 rare-earth honeycomb compound YbCl_3 , *Phys. Rev. B* **102**, 014427 (2020).
- [3] C. Broholm, R. J. Cava, S. A. Kivelson, D. G. Nocera, M. R. Norman, and T. Senthil, Quantum spin liquids, *Science* **367**, 263 (2020).
- [4] M. J. P. Gingras and P. A. McClarty, Quantum spin ice: A search for gapless quantum spin liquids in pyrochlore magnets, *Rep. Prog. Phys.* **77**, 056501(2014).
- [5] J. G. Rau and M. J. P. Gingras, Frustrated quantum rare-earth pyrochlores, *Annu. Rev. Condens. Matter Phys.* **10**, 357 (2019).
- [6] J. A. M. Paddison, H. S. Ong, J. O. Hamp, P. Mukherjee, X. Bai, M. G. Tucker, N. P. Butch, C. Castelnovo, M. Mourigal, and S. E. Dutton, Emergent order in the kagome Ising magnet $\text{Dy}_3\text{Mg}_2\text{Sb}_3\text{O}_{14}$, *Nat. Commun.* **7**, 13842 (2016).
- [7] R. Bag, M. Ennis, C. Liu, S. E. Dissanayake, Z. Shi, J. Liu, L. Balents, and S. Haravifard, Realization of quantum dipoles

- in triangular lattice crystal $\text{Ba}_3\text{Yb}(\text{BO}_3)_3$, *Phys. Rev. B* **104**, L220403 (2021).
- [8] J. Hamp, R. Moessner, and C. Castelnovo, Supercooling and fragile glassiness in a dipolar kagome Ising magnet, *Phys. Rev. B* **98**, 144439 (2018).
- [9] J. Colbois, B. Vanhecke, L. Vanderstraeten, A. Smerald, and F. Verstraete, Partial lifting of degeneracy in the J_1 - J_2 - J_3 Ising antiferromagnet on the kagome lattice, *Phys. Rev. B* **106**, 174403 (2022).
- [10] H. Komatsu, Y. Nonomura, and M. Nishino, Phase diagram of the dipolar Ising ferromagnet on a kagome lattice, *Phys. Rev. B* **106**, 014402 (2022).
- [11] S. L. Bud'ko, E. Morosan, and P. C. Canfield, Magnetic field induced non-Fermi-liquid behavior in YbAgGe single crystals, *Phys. Rev. B* **69**, 014415 (2004).
- [12] E. Morosan, S. L. Bud'ko, and P. C. Canfield, Angular-dependent planar metamagnetism in the hexagonal compounds TbPtIn and TmAgGe , *Phys. Rev. B* **71**, 014445 (2005).
- [13] S. Nakamura, S. Toyoshima, N. Kabeya, K. Katoh, T. Nojima, and A. Ochiai, Low-temperature properties of the $S = 1/2$ spin system $\text{Yb}_3\text{Ru}_4\text{Al}_{12}$ with a distorted kagome lattice structure, *Phys. Rev. B* **91**, 214426 (2015).
- [14] D. I. Gorbunov, M. S. Henriques, A. V. Andreev, V. Eigner, A. Gukasov, X. Fabrèges, Y. Skourski, V. Petříček, and J. Wosnitza, Magnetic anisotropy and reduced neodymium magnetic moments in $\text{Nd}_3\text{Ru}_4\text{Al}_{12}$, *Phys. Rev. B* **93**, 024407 (2016).
- [15] A. Dönni, G. Ehlers, H. Maletta, P. Fischer, H. Kitazawa, and M. Zolliker, Geometrically frustrated magnetic structures of the heavy-fermion compound CePdAl studied by powder neutron diffraction, *J. Phys.: Condens. Matter* **8**, 11213 (1996).
- [16] S. Lucas, K. Grube, C. L. Huang, A. Sakai, S. Wunderlich, E. L. Green, J. Wosnitza, V. Fritsch, P. Gegenwart, O. Stockert, and H. v. Löhneysen, Entropy evolution in the magnetic phases of partially frustrated CePdAl , *Phys. Rev. Lett.* **118**, 107204 (2017).
- [17] S. Paschen and Q. Si, Quantum phases driven by strong correlations, *Nat. Rev. Phys.* **3**, 9 (2021).
- [18] M. B. Sanders, J. W. Krizan, and R. J. Cava, $\text{RE}_3\text{Sb}_3\text{Zn}_2\text{O}_{14}$ ($\text{RE} = \text{La}, \text{Pr}, \text{Nd}, \text{Sm}, \text{Eu}, \text{Gd}$): A new family of pyrochlore derivatives with rare earth ions on a 2D kagome lattice, *J. Mater. Chem. C* **4**, 541 (2016).
- [19] A. Scheie, M. Sanders, J. Krizan, Y. Qiu, R. J. Cava, and C. Broholm, Effective spin-1/2 scalar chiral order on kagome lattices in $\text{Nd}_3\text{Sb}_3\text{Mg}_2\text{O}_{14}$, *Phys. Rev. B* **93**, 180407(R) (2016).
- [20] Z. L. Dun, J. Trinh, K. Li, M. Lee, K. W. Chen, R. Baumbach, Y. F. Hu, Y. X. Wang, E. S. Choi, B. S. Sharstry, A. P. Ramirez, and H. D. Zhou, Magnetic ground states of the rare-earth tripod kagome lattice $\text{Mg}_2\text{RE}_3\text{Sb}_3\text{O}_{14}$ ($\text{RE} = \text{Gd}, \text{Dy}, \text{Er}$), *Phys. Rev. Lett.* **116**, 157201 (2016).
- [21] A. Scheie, S. Dasgupta, M. Sanders, A. Sakai, Y. Matsumoto, T. R. Prisk, S. Nakatsuji, R. J. Cava, and C. Broholm, Homogeneous reduced moment in a gapful scalar chiral kagome antiferromagnet, *Phys. Rev. B* **100**, 024414 (2019).
- [22] P. Bordet, I. Gelard, K. Marty, A. Ibanez, J. Robert, V. Simonet, B. Canals, R. Ballou, and P. Lejay, Magnetic frustration on a kagome lattice in $\text{R}_3\text{Ga}_5\text{SiO}_{14}$ langasites with $\text{R} = \text{Nd}, \text{Pr}$, *J. Phys.: Condens. Matter* **18**, 5147 (2006).
- [23] A. Zorko, F. Bert, P. Mendels, P. Bordet, P. Lejay, and J. Robert, Easy-axis kagome antiferromagnet: Local-probe study of $\text{Nd}_3\text{Ga}_5\text{SiO}_{14}$, *Phys. Rev. Lett.* **100**, 147201 (2008).
- [24] S. Ghosh, S. Datta, H. Zhou, M. Hoch, C. R. Wiebe, P. Schlottmann, and S. Hill, Microwave-induced excitations in the kagome system $\text{Pr}_3\text{Ga}_5\text{SiO}_{14}$, *Phys. Rev. B* **88**, 094414 (2013).
- [25] Q. J. Li, Z. Y. Zhao, H. D. Zhou, W. P. Ke, X. M. Wang, C. Fan, X. G. Liu, L. M. Chen, X. Zhao, and X. F. Sun, Paramagnetic ground state with field-induced partial order in $\text{Nd}_3\text{Ga}_5\text{SiO}_{14}$ probed by low-temperature heat transport, *Phys. Rev. B* **85**, 174438 (2012).
- [26] X. S. Xu, T. V. Brinzari, S. McGill, H. D. Zhou, C. R. Wiebe, and J. L. Musfeldt, Absence of spin liquid behavior in $\text{Nd}_3\text{Ga}_5\text{SiO}_{14}$ using magneto-optical spectroscopy, *Phys. Rev. Lett.* **103**, 267402 (2009).
- [27] V. Simonet, R. Ballou, J. Robert, B. Canals, F. Hippert, P. Bordet, P. Lejay, P. Fouquet, J. Ollivier, and D. Braithwaite, Hidden magnetic frustration by quantum relaxation in anisotropic Nd Langasite, *Phys. Rev. Lett.* **100**, 237204 (2008).
- [28] Z. Ma, Z. Y. Dong, S. Wu, Y. Zhu, S. Bao, Z. Cai, W. Wang, Y. Shangguan, J. Wang, K. Ran, D. Yu, G. Deng, R. A. Mole, H. F. Li, S. L. Yu, J. X. Li, and J. S. Wen, Disorder-induced spin-liquid-like behavior in kagome-lattice compounds, *Phys. Rev. B* **102**, 224415 (2020).
- [29] Z. L. Dun, J. Trinh, M. Lee, E. S. Choi, K. Li, Y. F. Hu, Y. X. Wang, N. Blanc, A. P. Ramirez, and H. D. Zhou, Structural and magnetic properties of two branches of the tripod-kagome-lattice family $\text{A}_2\text{R}_3\text{Sb}_3\text{O}_{14}$ ($\text{A} = \text{Mg}, \text{Zn}$; $\text{R} = \text{Pr}, \text{Nd}, \text{Gd}, \text{Tb}, \text{Dy}, \text{Ho}, \text{Er}, \text{Yb}$), *Phys. Rev. B* **95**, 104439 (2017).
- [30] S. Sachdev, *Quantum Phase Transitions*, 2nd ed. (Cambridge University Press, Cambridge, England, 2011).
- [31] M. Vojta, Frustration and quantum criticality, *Rep. Prog. Phys.* **81**, 064501 (2018).
- [32] A. C. Y. Fang, S. R. Dunsiger, A. Pal, K. Akintola, J. E. Sonier, and E. Mun, Magnetic field induced effects in the quasikagome Kondo lattice system CePtPb , *Phys. Rev. B* **100**, 024404 (2019).
- [33] I. Ishii, T. Mizuno, K. Takezawa, S. Kumano, Y. Kawamoto, T. Suzuki, D. I. Gorbunov, M. S. Henriques, and A. V. Andreev, Magnetic-field-induced quadrupolar ordering and the crystal electric field effect in the distorted kagome lattice antiferromagnet $\text{Dy}_3\text{Ru}_4\text{Al}_{12}$, *Phys. Rev. B* **97**, 235130 (2018).
- [34] Y. Tokiwa, M. Garst, P. Gegenwart, S. L. Bud'ko, and P. C. Canfield, Quantum bicriticality in the heavy-fermion metamagnet YbAgGe , *Phys. Rev. Lett.* **111**, 116401 (2013).
- [35] Y. Tokiwa, C. Stingl, M. Kim, T. Takabatake, and P. Gegenwart, Characteristic signatures of quantum criticality driven by geometric frustration, *Sci. Adv.* **1**, e1500001 (2015).
- [36] H. Zhao, J. Zhang, M. Lyu, S. Bachus, Y. Tokiwa, P. Gegenwart, S. Zhang, J. Cheng, Y. Yang, G. Chen, Y. Ishikawa, Q. Si, F. Steglich, and P. Sun, Quantum-critical phase from frustrated magnetism in a strongly correlated metal, *Nat. Phys.* **15**, 1261 (2019).
- [37] M. Ashtar, J. Guo, Z. Wan, Y. Wang, G. Gong, Y. Liu, Y. Su, and Z. Tian, A new family of disorder-free rare-earth-based kagome lattice magnets: Structure and magnetic characterizations of RE_3BWO_9 ($\text{RE} = \text{Pr}, \text{Nd}, \text{Gd-Ho}$) boratotungstates, *Inorg. Chem.* **59**, 5368 (2020).
- [38] K. Y. Zeng, F. Y. Song, Z. M. Tian, Q. Chen, S. Wang, B. Liu, S. Li, L. S. Ling, W. Tong, L. Ma, and L. Pi, Local evidence for collective spin excitations in the distorted kagome antiferromagnet Pr_3BWO_9 , *Phys. Rev. B* **104**, 155150 (2021).

- [39] A. Majchrowski, E. Michalski, and A. Brenier, Growth and spectroscopic characterization of Nd_3BWO_9 single crystal, *J. Cryst. Growth* **247**, 467 (2003).
- [40] See Supplemental Material at <http://link.aps.org/supplemental/10.1103/PhysRevB.108.214410> for the structure refinement results of Nd_3BWO_9 single crystals, the constructed magnetic phase diagrams, and its comparison with the low-temperature $M(B)$ and $T(B)$ curves with B along the c and axes.
- [41] A. Podlesnyak, S. Rosenkranz, F. Fauth, W. Marti, A. Furrer, A. Mirmelstein, and H. J. Scheel, Crystal-field and magnetic properties of the distorted perovskite NdGaO_3 , *J. Phys.: Condens. Matter* **5**, 8973 (1993).
- [42] H. Yoshida, Y. Okamoto, T. Tayama, T. Sakakibara, M. Tokunaga, A. Matsuo, Y. Narumi, K. Kindo, M. Yoshida, M. Takigawa, and Z. Hiroi, Magnetization “steps” on a kagome lattice in volborthite, *J. Phys. Soc. Jpn.* **78**, 043704 (2009).
- [43] O. Janson, S. Furukawa, T. Momoi, P. Sindzingre, J. Richter, and K. Held, Magnetic behavior of volborthite $\text{Cu}_3\text{V}_2\text{O}_7(\text{OH})_2 \cdot 2\text{H}_2\text{O}$ determined by coupled trimers rather than frustrated chains, *Phys. Rev. Lett.* **117**, 037206 (2016).
- [44] D. Nakamura, T. Yamashita, H. Ishikawa, Z. Hiroi, and S. Takeyama, Extremely wide $1/3$ magnetic plateau of volborthite $\text{Cu}_3\text{V}_2\text{O}_7(\text{OH})_2 \cdot 2\text{H}_2\text{O}$ in ultrahigh magnetic field up to 182 T, *Phys. Rev. B* **98**, 020404(R) (2018).
- [45] M. Gen and H. Suwa, Nematicity and fractional magnetization plateaus induced by spin-lattice coupling in the classical kagome-lattice Heisenberg antiferromagnet, *Phys. Rev. B* **105**, 174424 (2022).
- [46] F. A. G. Albarracín, D. C. Cabra, H. D. Rosales, and G. L. Rossini, Spin-phonon induced magnetic order in the kagome ice, *Phys. Rev. B* **88**, 184421 (2013).
- [47] K. Y. Povarov, L. Facheris, S. Velja, D. Blosser, Z. Yan, S. Gvasaliya, and A. Zheludev, Magnetization plateaus cascade in the frustrated quantum antiferromagnet Cs_2CoBr_4 , *Phys. Rev. Res.* **2**, 043384 (2020).
- [48] K. S. Liu and M. E. Fisher, Quantum lattice gas and the existence of a supersolid, *J. Low Temp. Phys.* **10**, 516 (1973).
- [49] M. E. Fisher and D. R. Nelson, Spin flop, supersolids, and bicritical and tetracritical points, *Phys. Rev. Lett.* **32**, 1350 (1974).
- [50] A. S. Ferreira, M. A. Continentino, and E. C. Marino, Quantum corrections to the phase diagram of heavy-fermion superconductors, *Phys. Rev. B* **70**, 174507 (2004).
- [51] P. Coleman and A. H. Nevidomskyy, Frustration and the Kondo effect in heavy fermion materials, *J. Low. Temp. Phys.* **161**, 182 (2010).
- [52] J. M. Kosterlitz, D. R. Nelson, and M. E. Fisher, Bicritical and tetracritical points in anisotropic antiferromagnetic systems, *Phys. Rev. B* **13**, 412 (1976).
- [53] A. D. Bruce and A. Aharony, Coupled order parameters, symmetry-breaking irrelevant scaling fields, and tetracritical points, *Phys. Rev. B* **11**, 478 (1975).
- [54] F. Weickert, P. Gegenwart, C. Geibel, W. Assmus, and F. Steglich, Observation of two critical points linked to the high-field phase B in CeCu_2Si_2 , *Phys. Rev. B* **98**, 085115 (2018).
- [55] T. Giamarchi, C. Rüegg, and O. Tchernyshyov, Bose-Einstein condensation in magnetic insulators, *Nat. Phys.* **4**, 198 (2008).
- [56] S. Allenspach, P. Puphal, J. Link, I. Heinmaa, E. Pomjakushina, C. Krellner, J. Lass, G. S. Tucker, C. Niedermayer, S. Imaja, Y. Kohama, K. Kindo, S. Krämer, M. Horvatić, M. Jaime, A. Madsen, A. Mira, N. Laflorcier, F. Mila, B. Normand, C. Rüegg, R. Stern, and F. Weickert, Revealing three-dimensional quantum criticality by Sr substitution in Han purple, *Phys. Rev. Res.* **3**, 023177 (2021).
- [57] T. Radu, H. Wilhelm, V. Yushankhai, D. Kovrizhin, R. Coldea, Z. Tylczynski, T. Lühmann, and F. Steglich, Bose-Einstein condensation of magnons in Cs_2CuCl_4 , *Phys. Rev. Lett.* **95**, 127202 (2005).
- [58] M. Garst and A. Rosch, Sign change of the Grüneisen parameter and magnetocaloric effect near quantum critical points, *Phys. Rev. B* **72**, 205129 (2005).
- [59] Y. Kohama, High-field calorimetric studies on low-dimensional and frustrated quantum magnets, *J. Phys. Soc. Jpn.* **91**, 101004 (2022).
- [60] T. Liu, X. Y. Liu, Y. Gao, H. Jin, J. He, X. L. Sheng, W. Jin, Z. Chen, and W. Li, Significant inverse magnetocaloric effect induced by quantum criticality, *Phys. Rev. Res.* **3**, 033094 (2021).
- [61] K. Mochizuki, Y. Shimizu, A. Kondo, S. Nakamura, S. Kittaka, Y. Kono, T. Sakakibara, Y. Ikeda, Y. Isikawa, and K. Kindo, Thermodynamic investigation of metamagnetic transitions and partial disorder in the quasi-kagome Kondo lattice CePdAl , *J. Phys. Soc. Jpn.* **86**, 034709 (2017).
- [62] D. Flavian, J. Nagl, S. Hayashida, M. Yan, O. Zaharko, T. Fennell, D. Khalyavin, Z. Yan, S. Gvasaliya, and A. Zheludev, Magnetic phase diagram of the breathing-kagome antiferromagnet Nd_3BWO_9 , *Phys. Rev. B* **107**, 174406 (2023).
- [63] J. L. Jiménez, S. P. G. Crone, E. Fogh, M. E. Zayed, R. Lortz, E. Pomjakushina, K. Conder, A. M. Läuchli, L. Weber, S. Wessel, A. Honecker, B. Normand, Ch. Rüegg, P. Corboz, H. M. Rønnow, and F. Mila, A quantum magnetic analogue to the critical point of water, *Nature (London)* **592**, 370 (2021).
- [64] N. Tang, Y. Gritsenko, K. Kimura, S. Bhattacharjee, A. Sakai, M. Fu, H. Takeda, H. Man, K. Sugawara, Y. Matsumoto, Y. Shimura, J. Wen, C. Broholm, H. Sawa, M. Takigawa, T. Sakakibara, S. Zherlistyn, J. Wosnitzer, R. Moessner, and S. Nakatsuji, Spin-orbital liquid state and liquid-gas metamagnetic transition on a pyrochlore lattice, *Nat. Phys.* **19**, 92 (2023).
- [65] A. Andreanov and M. V. Fistul, Frustration-induced highly anisotropic magnetic patterns in the classical XY model on the kagome lattice, *Phys. Rev. B* **102**, 140405(R) (2020).
- [66] A. Aharony, Tetracritical points in mixed magnetic crystals, *Phys. Rev. Lett.* **34**, 590 (1975).
- [67] A. Pelissetto and E. Vicari, Multicritical behavior of two-dimensional anisotropic antiferromagnets in a magnetic field, *Phys. Rev. B* **76**, 024436 (2007).